



HAL
open science

Topography associated with crustal flow in continental collisions, with application to Tibet

Rebecca Bendick, D. Mckenzie, Jocelyn Etienne

► **To cite this version:**

Rebecca Bendick, D. Mckenzie, Jocelyn Etienne. Topography associated with crustal flow in continental collisions, with application to Tibet. *Geophysical Journal International*, 2008, 175, pp.375-385. 10.1111/j.1365-246X.2008.03890.x . inria-00384392

HAL Id: inria-00384392

<https://inria.hal.science/inria-00384392>

Submitted on 15 May 2009

HAL is a multi-disciplinary open access archive for the deposit and dissemination of scientific research documents, whether they are published or not. The documents may come from teaching and research institutions in France or abroad, or from public or private research centers.

L'archive ouverte pluridisciplinaire **HAL**, est destinée au dépôt et à la diffusion de documents scientifiques de niveau recherche, publiés ou non, émanant des établissements d'enseignement et de recherche français ou étrangers, des laboratoires publics ou privés.

Topography associated with crustal flow in continental collisions, with application to Tibet

R. Bendick,¹ D. M^cKenzie² and J. Etienne³

¹Department of Geology, University of Montana, 32 Campus Dr., Missoula, MT 59812-1296, USA. E-mail bendick@mso.umt.edu

²Bullard Laboratories, University of Cambridge, Madingley Road, Cambridge, CB3 0EZ, UK

³Laboratoire de Spectrometrie Physique, Universite J. Fourier CNRS, 140 av. de la Physique, Saint-Martin-d'Herès, France

Accepted 2008 June 13. Received 2008 June 13; in original form 2007 October 1

SUMMARY

Collision between an undeformable indenter and a viscous region generates isostatically compensated topography by solid-state flow. We model this process numerically, using a finite element scheme. The slope, amplitude and symmetry of the topographic signal depend on the indenter size and the Argand number of the viscous region, a dimensionless ratio of gravitational body forces to viscous forces. When applied to convergent continental settings, these scaling rules provide estimates of the position of an indenter at depth and the mechanical properties of the viscous region, especially effective viscosity. In Tibet, forward modelling suggests that some elevated, low relief topography within the northern plateau may be attributed to lower crustal flow, stimulated by a crustal indenter, possibly Indian lithosphere. The best-fit model constrains the northernmost limit of this indenter to 33.7°N and the maximum effective viscosity of Eurasian middle and lower crust to $1 \times 10^{20} \pm 0.3 \times 10^{20}$ Pa s.

Key words: Numerical solutions; Continental tectonics: compressional; Dynamics of lithosphere and mantle; Asia.

1 INTRODUCTION

Persistent topography on Earth is the sum of signals from a variety of tectonic and erosional processes, expressed over a wide range of spatial scales. The length scale of these signals can be used to decipher their likely cause. For example, high-amplitude, short-wavelength topography must be supported by stresses in the strong upper crust, with the topography itself being generated by tectonics and erosion. Such elastic flexure supports features with characteristic wavelengths, dependant on flexural rigidity; folding and brittle faulting produce surface displacements, with scaling characteristics that also depend on crustal rheology. The thickness of the elastic layer can also be estimated from the vertical distribution of seismic moment release in the continental crust (Maggi *et al.* 2000; Jackson *et al.* 2004), correlations between gravity and topographic loads (Burov & Diament 1995; M^cKenzie 2003), continental heat flow (M^cKenzie *et al.* 2005), seismic wave velocity (e.g. Shapiro & Ritzwoller 2002) and rock mechanics (Brace & Kohlstedt 1980). Beneath Tibet, we assume that the part of the crust that behaves as a viscous fluid is everywhere overlain by a thin lid of elastic uppermost crust. The observed relationship between gravity and topography (Braitenberg *et al.* 2003) and flexural modelling (Masek *et al.* 1994) require this elastic lid to have a thickness of less than 10 km beneath the Qiangtang terrain. Therefore, at the wavelengths with which we are concerned, of between 100 and 500 km, the elastic layer has little effect on the vertical motions. It is, however, sufficiently strong to impose a constant horizontal velocity at the upper surface. In contrast, the longest wavelength topographic

signals, such as the entire Tibetan Plateau, cannot be produced by deformation of the crust alone but must instead be the result of the deformation of the entire lithosphere (Houseman & England 1986; Royden 1996; Tapponnier *et al.* 2001; Vanderhaeghe *et al.* 2003; Thatcher 2006; Meade 2007).

Our concern, here, is with the intermediate scale contributions to surface topography from deeper parts of the crust, which are still poorly understood. Where the total crustal thickness is large, the deep parts of the crust are likely to deform as a viscous fluid (Royden 1996; Clark & Royden 2000; M^cKenzie & Jackson 2002; Beaumont *et al.* 2004). This deformation has the potential to generate persistent intermediate-wavelength topography that can be used to constrain the viscosity of the middle and lower crust.

We develop a 2-D continuum fluid model of the crustal behaviour in a continental collision, to test one mechanism for building intermediate-wavelength topography. The model is designed to incorporate three critical features: convergence, lateral rheological heterogeneity and rigid, deformable boundary conditions. These features are guided by independent geological and geophysical observations of the middle and lower crust in active tectonic settings. We model convergent conditions because continental shortening often produces a thick, mostly aseismic lower crust (e.g. Jackson *et al.* 2004), which is likely to undergo continuous deformation. We model lateral rheological heterogeneity because continental collision juxtaposes bodies of crustal material with differing temperatures and mechanical properties. Finally, we use boundary conditions that allow the upper surface of the crust and the Moho to change shape (Flesch *et al.* 2005; Bendick & Flesch 2007).

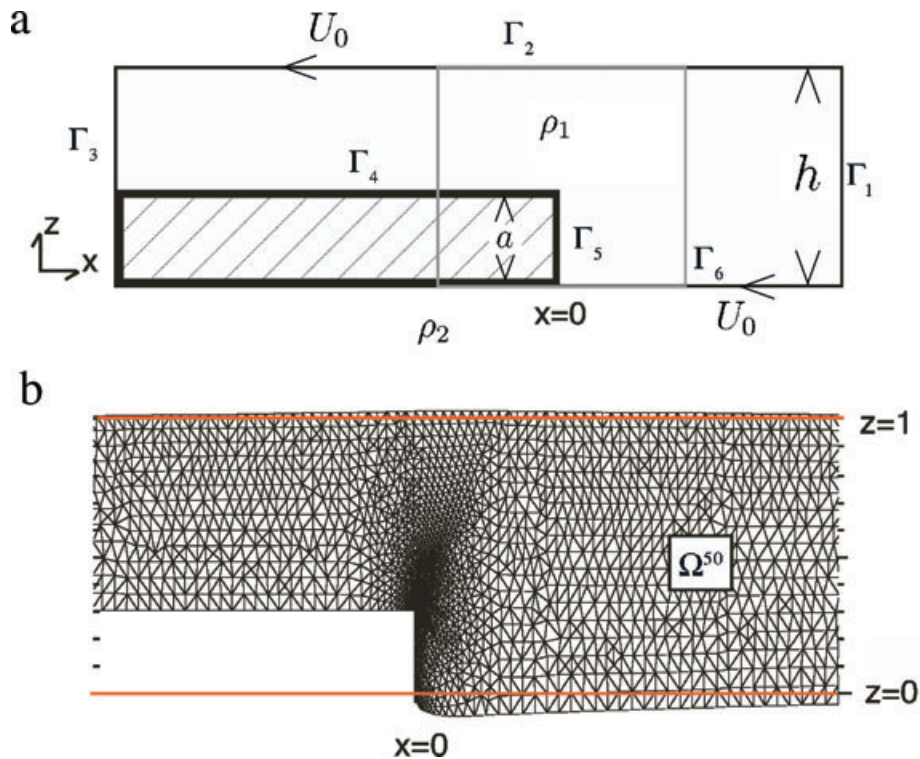


Figure 1. (a) Initial geometry for the numerical problem. The boundary conditions on labelled boundaries are discussed in the text. The heavy line outlines the region that is rigid and undeformable. (b) Deformed mesh at $t' = 50$. The mesh varies in density to accommodate regions of high strain. Γ_2 and Γ_6 are now deformed, as mesh nodes are advected during each iteration. Solutions for velocity and pressure are calculated at each iteration, for the entire region Ω .

Throughout this paper, ‘rigid’ is used to denote a boundary where the boundary-parallel velocity is specified, ‘free’ is one where the boundary-parallel stress is zero, ‘undeformable’ denotes one where boundary-normal velocity is specified to be zero and ‘deformable’ one where the boundary-normal stress is specified. Rigid, deformable boundary conditions, therefore, constrain parallel velocities and normal stresses on the boundaries of viscous regions in the crust. We use these boundary conditions to model the upper boundary of the crust because we are concerned with wavelengths that are large enough to be unaffected by flexural support. We believe that these conditions are appropriate for modelling the behaviour of Tibet, as India and Asia converge. Rigid, deformable boundary conditions permit crustal thickness changes to occur because the boundary conditions are on the vertical stress, and therefore, the boundaries are free to move vertically.

We consider a model in which a rigid sheet of thickness a is driven into a viscous layer of thickness h at a constant velocity U_0 (Fig. 1a). Where the upstream flow is unaffected by the motion of the rigid sheet, the velocity of the crust does not vary with depth, and the surface is horizontal. As the edge of the sheet passes below a point on the surface, the surface moves first up and then down, before again becoming horizontal far downstream from the edge of the sheet, where the velocity again becomes horizontal but now varies linearly with depth.

M^cKenzie *et al.* (2000) modelled the time-dependent behaviour of a viscous layer of viscosity η_1 and density ρ_1 overlying a half-space of viscosity η_2 and density $\rho_2 (> \rho_1)$, when the initial heights of the upper and lower boundaries of the layer, ξ and ζ , are given by $\xi_0 \sin kx$ and $\zeta_0 \sin kx$, where $k = 2\pi/\lambda$ is the wavenumber of the disturbance and λ is its wavelength. This system has two time constants. When $\xi_0 = \zeta_0$ and $kh \ll 1$, isostatic compensation oc-

curs with a time constant τ_b . The other mode is excited when $\xi_0 = -\zeta_0$, corresponding to variations in crustal thickness. These decay on a timescale of τ_a , due to lateral flow within the crust. When the viscosity of the half-space is much greater than that of the layer and the wavelength of the disturbance is large compared with the layer thickness, M^cKenzie *et al.* (2000) showed that $\tau_a \gg \tau_b$. A different form of behaviour occurs when $kh \gg 1$. Though there are still two time constants, they are associated with the relaxation of disturbances to the top and bottom surfaces of the layer. The time constants are only affected by the properties of the material on either side of the boundary concerned and are independent of the thickness of the layer. We are principally concerned with the topography of the upper surface of the layer and with wavelengths $\lambda < 6h$. M^cKenzie *et al.*’s calculations show that the time-dependent behaviour of the upper and lower surfaces are then essentially independent, and that the surface topography is scarcely affected by the boundary conditions imposed at the base of the layer.

We are concerned with the vertical motions of the surface as the edge of the sheet passes underneath. The behaviour of the model is principally controlled by the difference between the flux into the region from the right and that out to the left and by the relative thickness a/h of the sheet. The flux in from the right is $U_0 h$. Because the channel thickness on the left is $a - h$ and its base is stationary, Couette flow occurs, and the mass flux out to the left is $U_0(h - a)/2$. The difference between these fluxes is $U_0(h + a)/2$ and produces a bulge over the front edge of the sheet, which in turn generates gravity currents, which propagate upstream and downstream. Because the horizontal velocity of the upper surface is fixed, the shapes of the upstream and downstream bulges are different. The rate of uplift of the upper surface is affected by whether the base of the crust is rigid or deformable. However, the argument above suggests that its

shape is not, and this result was confirmed by changing the lower boundary condition from that in Fig. 1(a). Since we are concerned with the shape of the upper surface, rather than with the time taken to establish this shape, the choice of the lower boundary condition is unimportant.

We compare the results from this model with the topography of northern Tibet, where geophysical and geological evidence suggests that relatively strong Indian lower crust is intruding into thick, but relatively weak, Eurasian crust.

2 FLOW OVER A STEP

The model outlined in the previous section is most easily solved in a reference frame in which the front edge of the sheet is stationary. Conservation of mass and momentum in the layer then require

$$\nabla \cdot \mathbf{v} = 0, \quad (1)$$

$$\eta_1 \nabla^2 \mathbf{v} - \rho_1 g \hat{\mathbf{z}} - \nabla p = 0, \quad (2)$$

where $\mathbf{v} = (u, w)$ is the 2-D velocity, η_1 and ρ_1 are the viscosity and density of the layer of thickness h , g is the acceleration due to gravity, $\hat{\mathbf{z}}$ is a unit vector in the $+z$ direction and p is the pressure. The boundary conditions on the boundaries in Fig. 1(a) are

$$\begin{aligned} \mathbf{v} &= 0 \quad \text{on } \Gamma_4 \text{ and } \Gamma_5, \\ \mathbf{v} &= (-U_0, 0) \quad \text{on } \Gamma_1, \\ \mathbf{v} &= (-U_0 \left(\frac{z-a}{h-a} \right), 0) \quad \text{on } \Gamma_3, \end{aligned} \quad (3)$$

where U_0 is a constant. The boundary conditions on Γ_2 and Γ_6 are that they should be rigid and deformable, with $u = -U_0$ and that σ_{xz} is continuous on the deformed upper, ξ , and lower, ζ , boundaries.

Eqs (1) and (2) and the boundary conditions can be made dimensionless by substituting

$$\begin{aligned} \xi &= h\xi', \quad \zeta = h\zeta', \quad a = ha', \\ x &= hx', \quad z = hz', \quad \mathbf{v} = \frac{\rho_1 g h^2}{\eta_1} \mathbf{v}', \quad t = \frac{\eta_1}{\rho_1 g h} t', \\ p &= \rho_1 g h p', \quad \boldsymbol{\sigma} = \rho_1 g h \boldsymbol{\sigma}'. \end{aligned} \quad (4)$$

Eqs (1) and (2) and the boundary conditions then become

$$\nabla' \cdot \mathbf{v}' = 0, \quad (5)$$

$$\nabla'^2 \mathbf{v}' - \hat{\mathbf{z}} - \nabla' p' = 0, \quad (6)$$

$$\begin{aligned} \mathbf{v}' &= \left(-\frac{1}{Ar}, 0 \right) \quad \text{on } \Gamma_1, \\ \mathbf{v}' &= \left(-\frac{1}{Ar} \left(\frac{z'-a'}{1-a'} \right), 0 \right) \quad \text{on } \Gamma_3, \\ u' &= -\frac{1}{Ar} \quad \text{on } \Gamma_2 \text{ and } \Gamma_6, \\ -p' + 2 \frac{\partial w'}{\partial z'} &= 0 \quad \text{on } \Gamma_2 \end{aligned} \quad (7)$$

and

$$-p' + 2 \frac{\partial w'}{\partial z'} = R \zeta' \quad \text{on } \Gamma_6,$$

where Ar is the Argand number

$$Ar = \rho_1 g h^2 / \eta_1 U_0 \quad (8)$$

and

$$R = \rho_2 / \rho_1, \quad (9)$$

where ρ_2 is the density of the material underlying the layer. Ar measures the importance of the gravitational to the viscous forces.

Two kinematic boundary conditions require the rates of deformation on the upper and lower boundaries of the layer to equal their normal velocities:

$$\frac{d\xi'}{dt'} = w'_{z'=1} \quad \text{and} \quad \frac{d\zeta'}{dt'} = w'_{z'=0}. \quad (10)$$

Eqs (5) and (6) with the boundary conditions (7) and (10) were then solved using the finite element method with $\zeta' = \xi' = 0$, initially.

The numerical solution consists of a set of triangular tessellations (Fig. 1b), which approximate the domain Ω^n at time t^n , velocity fields \mathbf{v}^n and pressure fields p^n , which are continuous and, respectively, piecewise quadratic or linear polynomial functions over the triangles of Ω^n . This discretization is known as the Taylor–Hood finite element form (Hood & Taylor 1973) and is adequate for solving Stokes' problem (Brezzi & Fortin 1991).

The numerical algorithm increments in time and consists of three steps. As the approximations Ω^{n-1} and \mathbf{v}^{n-1} are known from the previous iteration, the z -coordinate of the mesh nodes of the boundaries Γ_2^n and Γ_6^n can be calculated to first-order accuracy, using the approximate velocity \mathbf{v}^{n-1} . Next, the nodes of mesh Ω^{n-1} are advected by a smooth function so that they form a new mesh Ω^n , with boundaries Γ_2^n and Γ_6^n . Then the velocity \mathbf{v}^n and pressure p^n are calculated over the new mesh, using the variational forms of eqs (5) and (6) with an augmented Lagrangian technique (Fortin & Glowinski 1983). This algorithm is implemented within the finite element environment RHEOLEF (Saramito *et al.* 2006).

We confirmed that solutions calculated in this way are insensitive to changes in the geometry of the triangular mesh and to changes in the time increment, by comparing numerical runs using different mesh and step sizes (Fig. 2a). No substantial differences in the shape of Γ_2 or Γ_6 occur, as long as the stability conditions are satisfied.

We also compared the numerical results with an analytical solution, which can be obtained when $a' = 1$ and when the boundary conditions on Γ_5 are that $u = 0$ and $\sigma_{xz} = 0$ (see Appendix). Because the numerical solution is unstable when $a' = 1$, we compared the analytic solution to the numerical solution with $a' = 0.9$. There is good agreement in the length and slope of the topography away from $x' = 0$ (Fig. 2b). As expected, near $x' = 0$ the solutions disagree because the tangential boundary conditions of the two models are different.

We then generated a number of numerical solutions, with different values of Ar and a/h (Fig. 3). The shape of the bulge can be described by its slope and a measure of its skewness, given by a ratio between the deformation length in the positive direction and the deformation length in the negative direction (inset in Fig. 4). The skewness of the topographic bulge is largely controlled by a/h , and its slope is principally controlled by the Argand number.

We fitted second-order polynomials that related the slope and skewness to the step ratio a/h and the Argand number by minimizing the root mean square (rms) misfits (Fig. 5). If $x = \ln Ar$ and $y = \ln(a/h)$, the slope of the surface displacement is described by

$$\ln(\xi'_{\max}/L'_e) = \sum_{m=0}^2 \sum_{n=0}^2 A_{mn} x^m y^n. \quad (11)$$

The coefficients that minimize the rms difference between ξ'_{\max}/L'_e calculated from eq. (11) and those from the numerical simulations are

$$\begin{aligned} A_{00} &= -1.5164, \quad A_{10} = 0.0574, \quad A_{01} = 1.3302, \\ A_{11} &= 0.0022, \quad A_{20} = -0.0987, \quad A_{02} = 0.5532, \end{aligned} \quad (12)$$

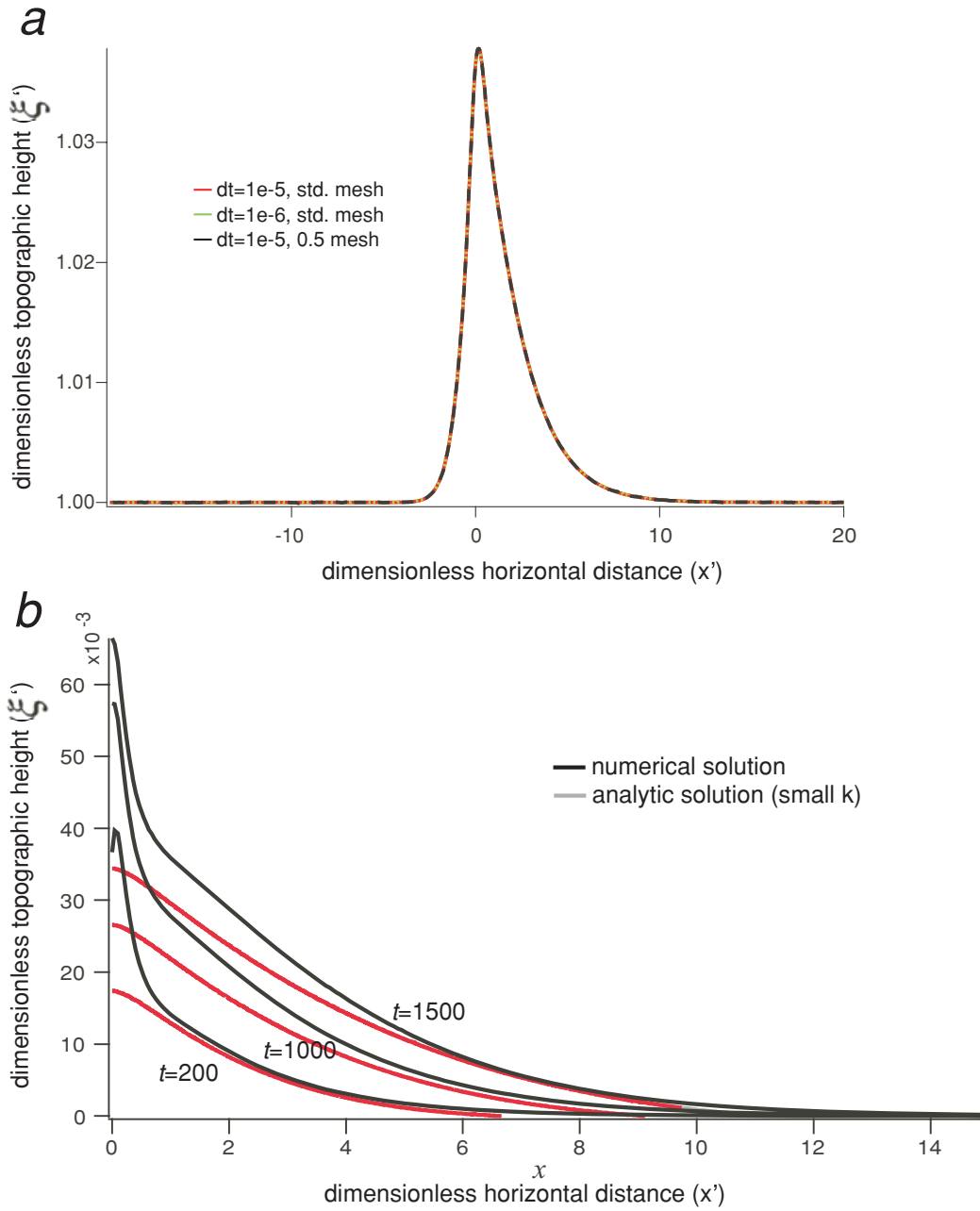


Figure 2. (a) Tests of sensitivity of the numerical solution to changes in mesh density and in the size of the time step. (b) Comparison of the surface deformation from the numerical model in Fig. 1 with that from the analytic solution in the Appendix. The behaviour of the two models near $x = 0$ is different because the boundary conditions on Γ_5 (see Fig. 1a) for the two models are different.

with

$$A_{21} = A_{12} = A_{22} = 0.$$

The skewness of the surface displacement is described by

$$\ln(L'_{\max}/L'_{\min}) = \sum_{m=0}^2 \sum_{n=0}^2 B_{mn} x^m y^n \quad (13)$$

and the corresponding coefficients are

$$\begin{aligned} B_{00} &= 2.9144, & B_{10} &= 0.2113, & B_{01} &= 3.3287, \\ B_{11} &= 0.0035, & B_{20} &= -0.0483, & B_{02} &= 1.2656, \end{aligned} \quad (14)$$

and

$$B_{21} = B_{12} = B_{22} = 0.$$

Expressions (11) and (13) can be solved simultaneously for real topographic features, produced by crustal flow to obtain estimates of Ar and the step ratio. Given estimates of density, layer thickness and convergence velocity, Ar and a/h then provide constraints on the viscosity and the step height.

3 APPLICATION TO TIBET

The map of the smoothed topography of the Tibetan Plateau shows that there is a low relief, high-elevation region between the

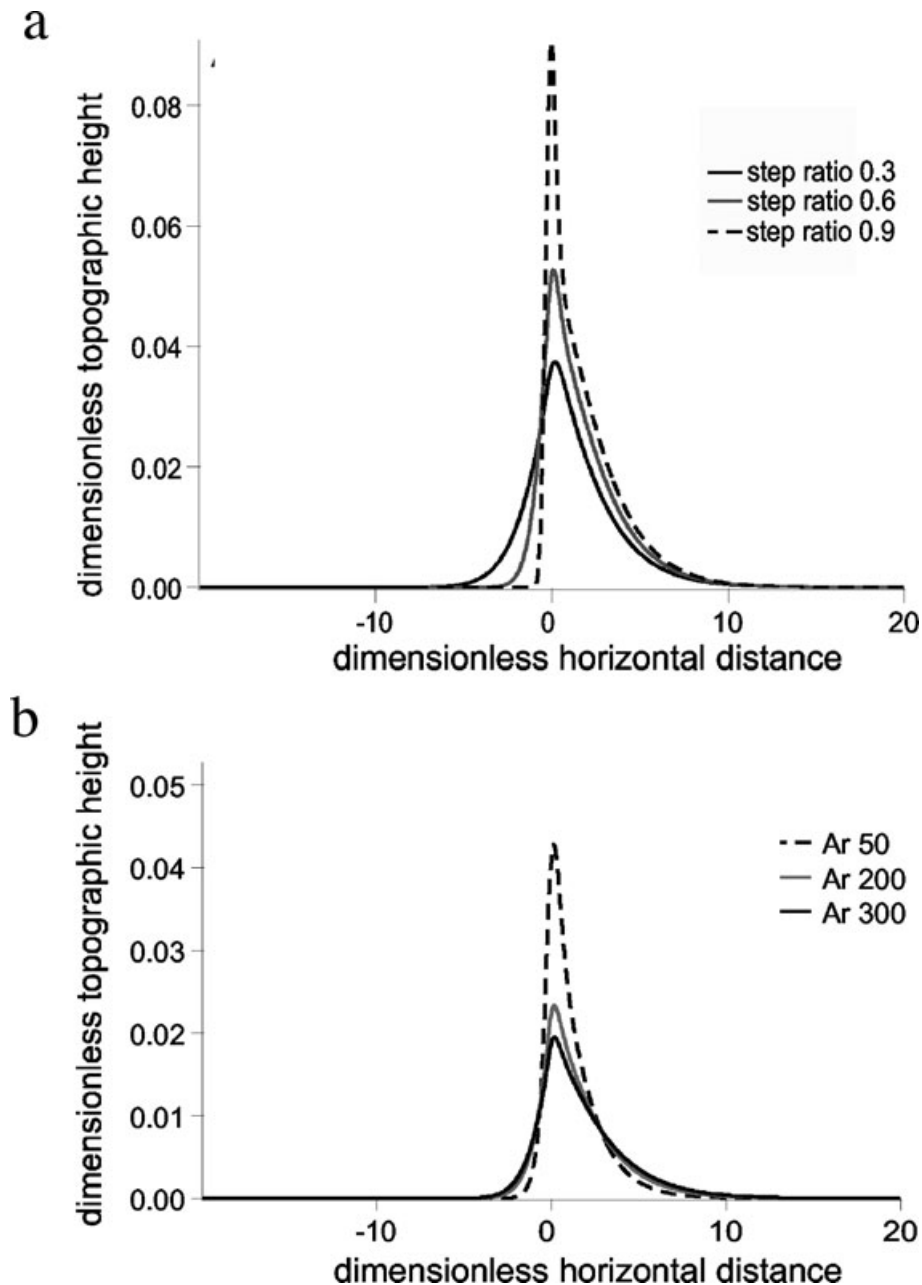


Figure 3. (a) Plots of topography for $Ar = 100$, after 10^5 iterations, to show the influence of the step ratio a/h . (b) Plots of topography for $a/h = 0.5$, after 10^5 iterations, to show the influence of the Argand number.

Banggong–Nujiang Suture (BNS) and the Altyn Tagh Fault (ATF), called the Qiangtang. This region is the highest part of Tibet and also has the lowest relief of any part of the Plateau (Fielding *et al.* 1994). We believe that the high elevation and low relief of the Qiangtang is the surface expression of flow in the lower crust.

A number of geophysical studies of the structural differences between southern and northern Tibet suggest that the the Indian Shield behaves as a rigid sheet with a step at its northern edge (Fig. 6), near the BNS. The Indian lower crustal indenter is thinner than the whole Eurasian crust, making the rheology of the southern Tibetan crust vertically heterogeneous, whereas that of the northern Tibetan crust is more nearly homogeneous.

In general, crust beneath the Qiangtang, north of the BNS, has a positive seismic velocity gradient with increasing depth but is,

everywhere, slower than average continental crust (Owens & Zandt 1997). INDEPTH III results support the presence of warm but dry crust to north of the BNS (Haines *et al.* 2003). Seismic wide-angle data also confirm that the lower crust north of the BNS has slow P -wave velocities, without a distinct low velocity layer (Meissner *et al.* 2004) and has an anomalously high Poisson's ratio (Owens & Zandt 1997). S_n is also strongly attenuated throughout most of the northern plateau (McNamara *et al.* 1995). Forward models of flexure give an upper bound on lower crustal viscosity in flat central and northern Tibet of $<10^{22}$ Pa s (Masek *et al.* 1994; Flesch *et al.* 2001). Fielding *et al.* (1994) infer a similarly low viscosity from the low average relief between BNS and the Altyn Tagh front. Strong polarization anisotropy of the upper mantle starts north of 32°N (McNamara *et al.* 1994; Huang *et al.* 2000) with little east–west

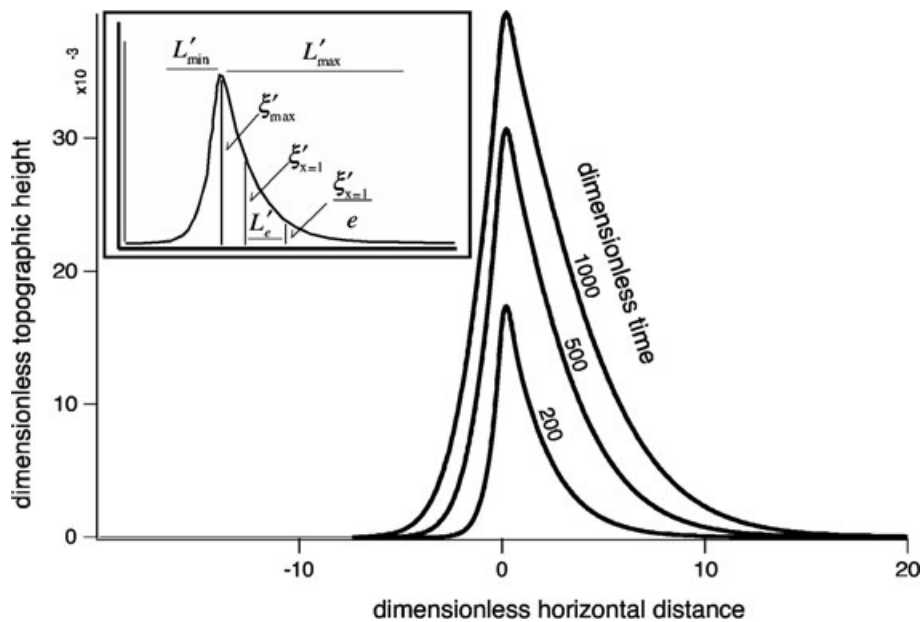


Figure 4. Numerical solutions for the topography for $Ar = 100$. The inset shows the various measures of topography used to parametrize the shape of the deformation. ξ'_{\max} is the maximum height of the bulge, which on the upstream side varies approximately exponentially at a sufficient distance from its maximum. A measure of the characteristic length scale L'_e of this part of the bulge was obtained by measuring the location x_1 at which the height of the bulge is $\xi'_{x=1}/e$, where $\xi'_{x=1}$ is the height of the bulge at $x' = 1$. L'_e is then defined as $x_1 - 1$. ξ'_{\max}/L'_e is approximately the same as the upstream slope. L'_{\max} and L'_{\min} are the distances from the step in the upstream and downstream directions where the dimensionless height of the bulge exceeds 5×10^{-6} .

variation. Flesch *et al.* (2005) argue that the correlation between the splitting direction in the mantle lithosphere and the direction of maximum shear strain in the upper crust requires the vertical stresses to be continuous through the entire lithosphere beneath the northern plateau.

South of the BNS, the crust contains a clear low velocity layer, probably between depths of 20–30 km, but perhaps with an upper limit as shallow as 10 km (Yuan *et al.* 1997) and a lower limit as deep as 60 km (Cotte *et al.* 1999). This layer has a high electrical conductivity between 15 and 20 km (Wei *et al.* 2001), as well as seismic bright spots. Both are interpreted as evidence of the presence of melt or saline fluids (Brown *et al.* 1996). Below ≈ 50 km, the lower crust and upper mantle are inferred to be Indian in origin. This region is believed to be strong because it has high P velocities (Owens & Zandt 1997) and the upper mantle lacks polarization anisotropy (Sandvol *et al.* 1997). DeCelles *et al.* (2002) estimate that this lower crustal slab of Indian lithosphere is 20 km thick, as do Jin *et al.* (1996), or much less than the total crustal thickness of at least 70 km (Kind *et al.* 2002; Mitra *et al.* 2005). The Indian lithosphere has negligible anisotropy everywhere south of the Himalayan Front (Sandvol *et al.* 1997).

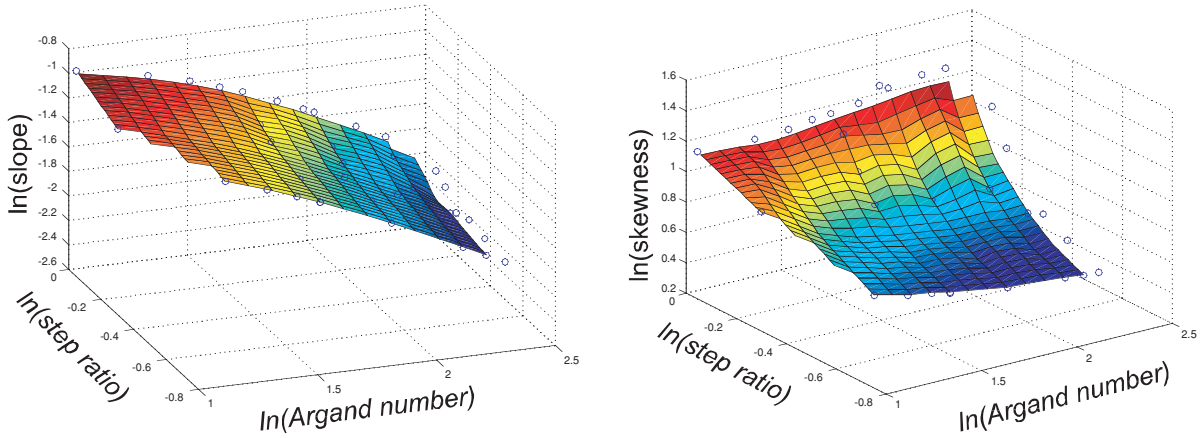
In summary (Fig. 6), a variety of arguments show that there is an important structural difference between southern and northern Tibet (Klemperer 2006). Northern Tibet is made entirely of relatively weak Eurasian crust, with a limited viscosity contrast across the Moho. Southern Tibet is made of a layer of weak material, sandwiched between cold Indian crust and mantle (Lyon-Caen & Molnar 1985) and an uppermost crust, thick enough to support topographic relief greater than 1 km (Fielding *et al.* 1994).

Channel flow is an appropriate model for southern Tibet, since the viscosity contrast between the low velocity crustal layer and the relatively thick, elastic uppermost crust is large, as is that between

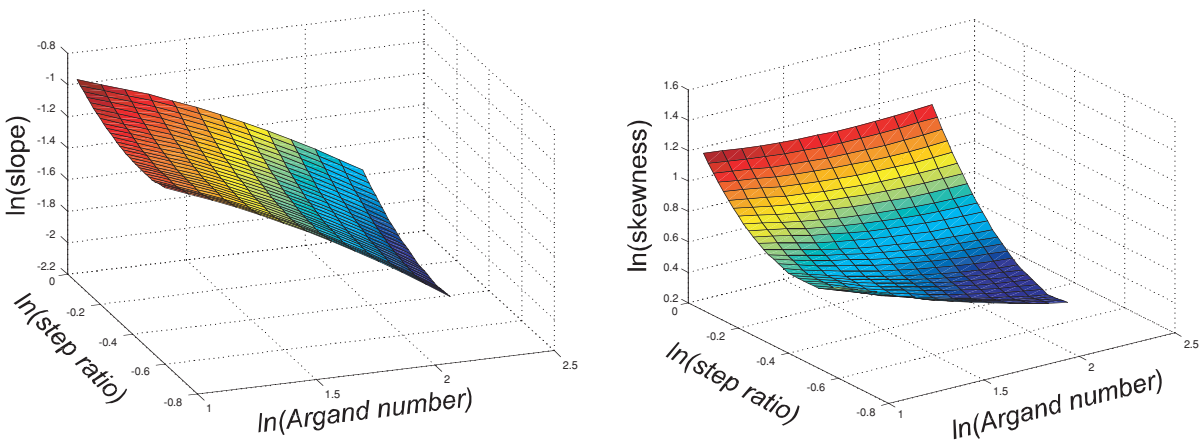
the low velocity crustal layer and the indenting Indian lower crust and mantle lithosphere. In northern Tibet, there are no large viscosity contrasts within the lower crust and lithosphere. The thin elastic upper crust has a low effective flexural rigidity (Masek *et al.* 1994), and the lower crust and mantle consist of Eurasian material, which does not support elastic stresses on geological timescales either because of the presence of small amounts of water (Hirth & Kohlstedt 1996) or because of the high temperature. The observations of S wave anisotropy also indicate a well-developed ductile fabric in the mantle (McNamara *et al.* 1994; Huang *et al.* 2000). The model in Fig. 1(a) is therefore likely to describe the major rheological properties of the crust beneath the Tibetan Plateau. Its behaviour is not sensitive to the exact shape of the front of the Indian indenter, which is likely to vary along strike.

The model can only be expected to reproduce the low-amplitude, intermediate-wavelength bulge produced by the collision between Indian and Tibetan lower crust. It will not reproduce the short-wavelength topography produced by deformation of the upper crust or long-wavelength topography produced by deformation of the whole lithosphere. The overall topography of the plateau is a sum of all deformation over a wide range of wavelengths. We, therefore, compare model topography to that of northern Tibet, by removing both long and short wavelength topography (Fig. 7). First, we account for the whole-lithosphere tectonics by adding the mean plateau elevation (4600 m) to the model topography. Second, we remove the short-wavelength upper crustal contribution from the real topography by stacking and averaging N–S sections at 3 s spacing, in a swath between 87°E and 90°E (Fig. 8). This swath includes only the region of the plateau where flow is most likely to be normal to the direction of convergence between India and Eurasia. Our model is 2-D, so, cannot account for E–W flow, which is especially important beneath eastern Tibet (Ozacar & Zandt 2004; Zhang *et al.* 2004).

data



second-order model



residuals

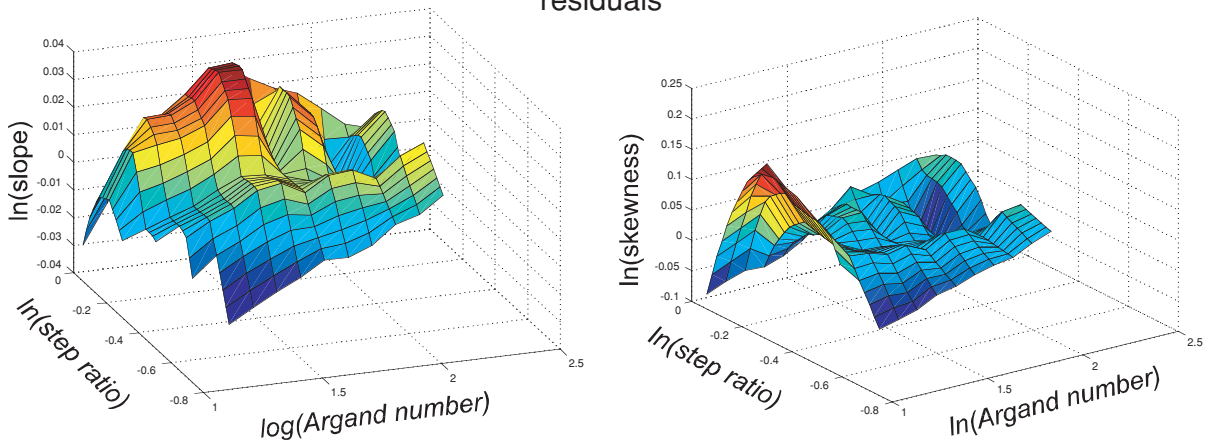


Figure 5. Surfaces fit to measurements of (a) the slope ξ'_{\max}/L'_e and (b) the skewness L'_{\max}/L'_{\min} of the topography from model runs as functions of step ratio and Argand number. The individual measurements are shown with open circles. Plots of the polynomial fits, eqs (3) and (4), to the measurements in (a) and (b). Residuals between the numerical results and the polynomial fits. Note the change in vertical scale between (a)–(d) and (e) and (f).

4 TIBETAN TOPOGRAPHY FROM CRUSTAL FLOW

The model and the observed, bandpassed topography both include a low-amplitude, long-wavelength bulge in the Qiangtang, north

of the Banggong Suture, which we interpret to be the topographic expression of crustal flow resulting from the Indian indenter. We believe that the relatively low elevation of the BNS (Fig. 7) marks the southern limit of topography excited by the intrusion of the rigid Indian crust and lithosphere. The absence of intermediate

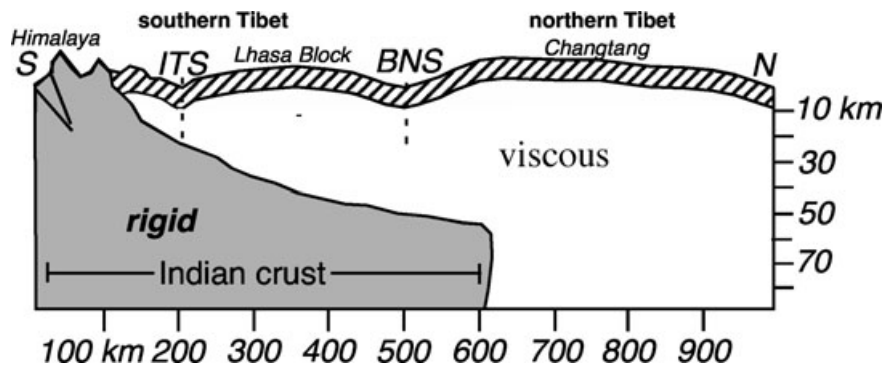


Figure 6. A cartoon cross-section showing lateral and vertical heterogeneity of the crust beneath Tibet. Rigid Indian crust and lithosphere penetrates Eurasian lower crust as far north as the Banggong–Nujiang Suture (BNS) region. In the southern plateau, a viscous crustal channel is confined between the Indian indenter and the thin elastic lid (hatched) at the surface. In the northern plateau, no strong viscosity contrast exists at depth.

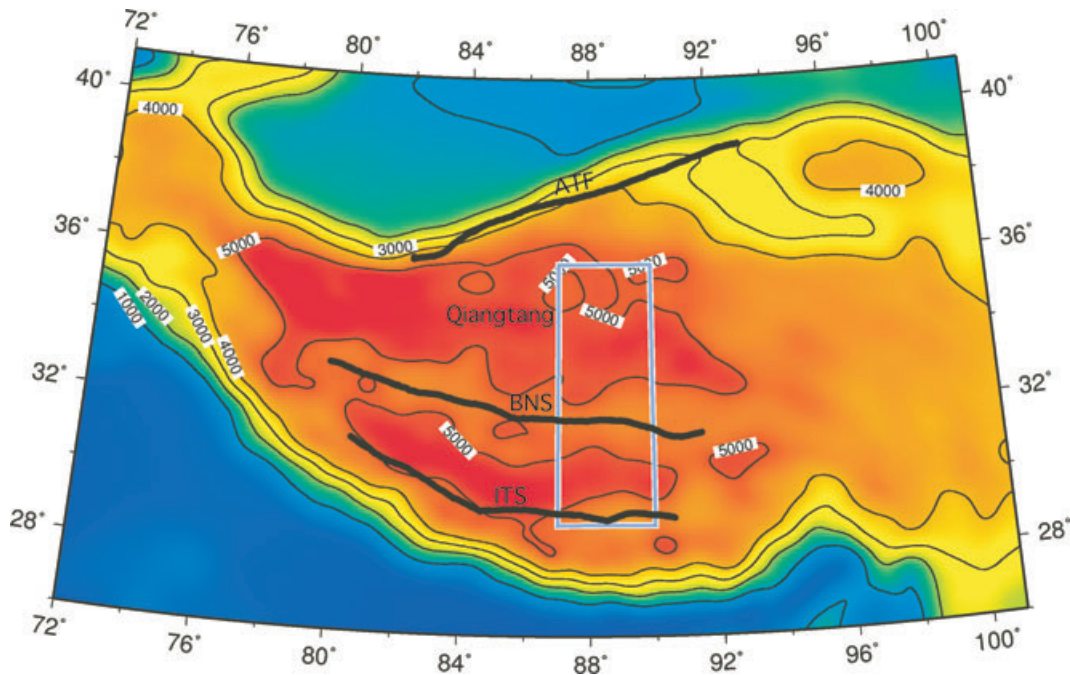


Figure 7. Smoothed topography of the Tibetan Plateau. The region dominated by crustal flow is the region of low relief in the centre of the plateau. The swath used to generate topographic profile in Fig. 8 is shown as a blue box and was produced by averaging N–S profiles from 29°N to 39°N between 87°E and 90°E. ITS, the Indus – Tsangpo suture; BNS, the Banggong–Nujiang suture and ATF, the Altyn Tagh fault.

wavelength topography south of this limit is compatible with horizontal flow in the crust, since only the vertical component of the velocity generates topography. The maximum elevation in the Qiangtang is located near 33.7°N. According to our model, this corresponds to the position of the front of the indenter. This is >100 km north of most estimates of the northernmost limit of Indian crust from seismic observations (e.g. Chen & Ozalaybey 1998; Tilmann *et al.* 2003; Ozacar & Zandt 2004).

The observed topographic profiles are used to estimate the position of the step and also Ar and relative step height through simultaneous solutions of eqs (11) and (13). The shape of the Qiangtang bulge constrains the values of $L_{\max} + L_{\min}$, the slope, ξ_{\max}/L_e , and the skewness, L_{\max}/L_{\min} . We used these estimates to calculate Ar and a/h , using eqs (11) and (13). This approach gives an Argand number of about 1500 and a dimensionless step height of 0.3. Using this value of Ar , we calculate the viscosity of the flowing crust from eq. (8) and estimates of the values of the other parameters. The mean

crustal density for central Tibet is taken to be 2.9 Mg m^{-3} (Haines *et al.* 2003) and g is 9.8 m s^{-2} . We estimate that the thickness of the viscous layer can be no more than 60 km because the published Moho depths for central Tibet range from 50–78 km (Zhao *et al.* 2001; Haines *et al.* 2003; Meissner *et al.* 2004) and the elastic lid thickness is <10 km (Masek *et al.* 1994). The total relative velocity between the Indian indenter and the Tibetan lower crust is $\approx 20 \text{ mm yr}^{-1}$. This value is less than the total India–Eurasia convergence rate of 28–34 mm yr^{-1} (Zhang *et al.* 2004) because some of the relative motion is taken up by deformation north of Tibet. If the Argand number is 1500, these values give a viscosity of the Tibetan middle and lower crust of 10^{20} Pa s , in general agreement with other bounds on crustal viscosity (Meissner & Kusznir 1987; Masek *et al.* 1994; Flesch *et al.* 2001; Copley & M^cKenzie 2007). The fit between the model and observed topography is satisfactory for Argand numbers between 1200 and 1700, corresponding to a viscosity range from 0.8×10^{20} to $1.1 \times 10^{20} \text{ Pa s}$. The thickness

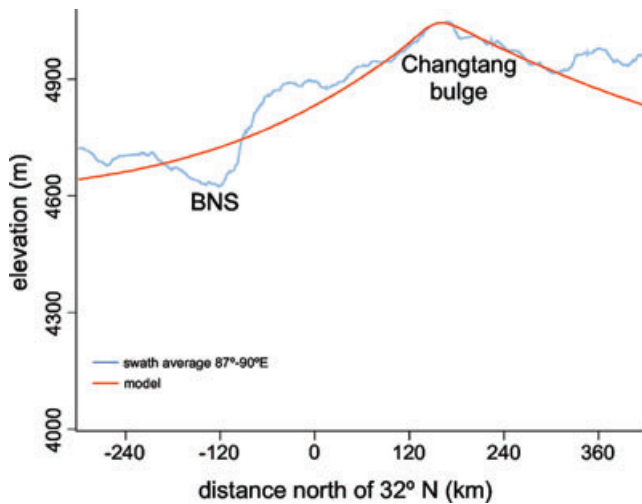


Figure 8. Mean topography of the Qiangtang bulge from the swath shown in Fig. 7 (blue), compared with the best fitting model (red) with $Ar=1500$, $a/h = 0.3$ and $h = 60$ km.

of the viscous region and the convergence velocity between the indenter and the Indian lower crust are probably the least well known of the parameters involved. Reasonable bounds on layer thickness are 40–60 km and between 15 and 30 mm yr^{-1} for the convergence velocity. Using these values, the acceptable range of lower crustal viscosities increases to $1 \times 10^{20} \pm 0.3 \times 10^{20}$ Pa s. A dimensionless step size of 0.3 gives a thickness for the Indian crustal indenter of 20 km, in agreement with independent estimates from seismology (Brown *et al.* 1996; Sandvol *et al.* 1997) and gravity (Jin *et al.* 1996). Our estimate of the viscosity of the low-viscosity layer beneath Tibet agrees with that of 10^{20} Pa s obtained by Copley & McKenzie (2007). They modelled the GPS velocities across the Himalayan front as a gravity-driven flow. They also showed that this value for the viscosity is compatible with the creep properties of crustal rocks at temperatures of 700–900 °C.

5 DISCUSSION

The models for crustal flow, under conditions of convergence presented here, apply to any region with compressive boundary conditions, where part of the crust is sufficiently weak for solid-state flow to occur and where the structure suggests that large lateral variations in rheology are present. The solutions we have obtained for lower crustal flow over a step require the vertical stress to be continuous through the lithosphere. The topographic effects of the flow described here are sufficiently large in amplitude to be observed at the surface and to be separated from both shorter wavelength features supported by elastic forces in the upper crust and longer wavelength features generated by distributed deformation of the whole lithosphere. The shape of topography supported by lower crustal flow can be used to estimate the geometry of a crustal indenter and the viscosity of the lower crust.

In the case of Tibet, a model of flow over a rigid, undeformable indenter reproduces the elevation, slope and asymmetry of the elevation in the Qiangtang region of Tibet, which is associated with the northern limit of Indian lithosphere. The model is 2-D, and therefore, cannot describe the eastward component of flow or any E–W variations in mechanical properties. The shape of the indenter is also likely to be more complicated than that modelled here and may vary significantly along strike. These 3-D effects may be

responsible for the discrepancy between seismic estimates of the geographic position of Indian lower crust and mantle lithosphere and our estimate from the topography.

The topography of northern Tibet sets an upper bound on the northern extent of the Indian indenter near 33.7°N and on the viscosity of the lower crust beneath northern Tibet of 1.3×10^{20} Pa s. The model also provides an estimate of 20 km for the thickness of the Indian crust that is present beneath southern Tibet.

ACKNOWLEDGMENTS

The NERC COMET programme supported this research. RB thanks J. Jackson, P. England, B. Parsons and J. Li for suggestions and support, A. Copley for generating Fig. 7 and L. Royden and C. Beaumont for their useful reviews.

REFERENCES

- Beaumont, C., Jamieson, R., Nguyen, M. & Medvedev, S., 2004. Crustal channel flows, 1: numerical models with applications to the tectonics of the Himalayan–Tibetan orogen, *J. geophys. Res.*, **109**, B06406.
- Bendick, R. & Flesch, L., 2007. Reconciling lithospheric deformation and lower crustal flow beneath central Tibet, *Geology*, **35**, 895–898.
- Brace, W. & Kohlstedt, D., 1980. Limits on lithospheric stress imposed by laboratory experiments, *J. geophys. Res.*, **85**, 6248–6252.
- Braitenberg, C., Wang, Y., Fang, J. & Hsu, H., 2003. Spatial variations of flexure parameters over the Tibet–Qinghai plateau, *Earth planet. Sci. Lett.*, **205**, 211–224.
- Brezzi, F. & Fortin, M., 1991. *Mixed and Hybrid Finite Elements Methods*, Springer-Verlag, New York.
- Brown, L. *et al.*, 1996. Bright spots, structure, and magmatism in southern Tibet from INDEPTH seismic reflection profiling, *Science*, **274**, 1688–1691.
- Burov, E. & Diament, M., 1995. The effective elastic thickness (T_e) of continental lithosphere: what does it really mean?, *J. geophys. Res.*, **100**, 3905–3927.
- Chen, W. & Ozalaybey, S., 1998. Correlation between seismic anisotropy and Bouguer gravity anomalies in Tibet and its implications for lithospheric structures, *Geophys. J. Int.*, **135**, 93–101.
- Clark, M. & Royden, L., 2000. Topographic ooze: building the eastern margin of Tibet by lower crustal flow, *Geology*, **28**, 703–706.
- Copley, A. & McKenzie, D., 2007. Models of crustal flow in the India–Asia collision zone, *Geophys. J. Int.*, **169**, 683–698.
- Cotte, N., Pedersen, H., Campillo, M., Mars, J., Ni, J., Kind, R., Sandvol, E. & Zhao, W., 1999. Determination of the crustal structure in southern Tibet by dispersion and amplitude analysis of Rayleigh waves, *Geophys. J. Int.*, **138**, 809–819.
- DeCelles, P., Robinson, D. & Zandt, G., 2002. Implications of shortening in the Himalayan fold-thrust belt for uplift of the Tibetan plateau, *Tectonics*, **21**, 1062.
- Fielding, E., Isacks, B., Barazangi, M. & Duncan, C., 1994. How flat is Tibet? *Geology*, **22**, 163–167.
- Flesch, L., Haines, A.J. & Holt, W., 2001. Dynamics of the India–Eurasia collision zone, *J. geophys. Res.*, **106**, 16 435–16 460.
- Flesch, L., Holt, W., Silver, P., Stephenson, M., Wang, C. & Chao, W., 2005. Constraining the extent of crust–mantle coupling in central Asia using GPS, geologic, and shear-wave splitting data, *Earth planet. Sci. Lett.*, **238**, 248–268.
- Fortin, M. & Glowinski, R., 1983. *Augmented Lagrangian Methods, Applications to the Numerical Solution of Boundary Value Problems*, Elsevier Science, Amsterdam.
- Haines, S., Klemperer, S., Brown, L., Guo, J., Mechie, J., Meissner, R., Ross, A. & Zhao, W., 2003. INDEPTH III seismic data: from surface observations to deep crustal processes in Tibet, *Tectonics*, **22**, 1001.

Hirth, G. & Kohlstedt, D., 1996. Water in the oceanic upper mantle: implications for rheology, melt extraction, and the evolution of the lithosphere, *Earth planet. Sci. Lett.*, **144**, 93–108.

Hood, P. & Taylor, C., 1973. A numerical solution of the Navier-Stokes equations using the finite element technique, *Comput. Fluids*, **1**, 73–100.

Houseman, G. & England, P., 1986. Finite strain calculations of continental deformation. 1: method and general results for convergent zones, *J. geophys. Res.*, **91**, 3651–3663.

Huang, W. *et al.*, 2000. Seismic polarization anisotropy beneath the central Tibetan Plateau, *J. geophys. Res.*, **105**, 27 979–27 989.

Jackson, J., Austrheim, H., M^cKenzie, D. & Priestley, K., 2004. Metastability, mechanical strength, and the support of mountain belts, *Geology*, **32**, 625–628.

Jin, Y., McNutt, M. & Zhu, Y., 1996. Mapping the descent of Indian and Eurasian plates beneath the Tibetan Plateau from gravity anomalies, *J. geophys. Res.*, **101**, 11 275–11 290.

Kind, R. *et al.*, 2002. Seismic images of crust and upper mantle beneath Tibet: evidence for Eurasian plate subduction, *Science*, **298**, 1219–1221.

Klemperer, S., 2006. Crustal flow in Tibet: geophysical evidence for the physical state of Tibetan lithosphere, and inferred patterns of active flow, in *Channel Flow, Ductile Extrusion, and Exhumation in Continental Collision Zones*, Vol. 268, p. 39–70, eds Law, R.D., Searle, M.P. & Godin, L., Spec. Publ. Geological Society, London.

Lyon-Caen, H. & Molnar, P., 1985. Gravity anomalies, flexure of the Indian Plate, and the structure, support and evolution of the Himalaya and Ganga Basin, *Tectonics*, **4**, 513–538.

Maggi, A., Jackson, J., M^cKenzie, D. & Priestley, K., 2000. Earthquake focal depths, effective elastic thickness, and the strength of the continental lithosphere, *Geology*, **28**, 495–498.

Masek, J., Isacks, B. & Fielding, E., 1994. Rift flank uplift in Tibet: evidence for a viscous lower crust, *Tectonics*, **13**, 659–667.

M^cKenzie, D., 2003. Estimating T_e in the presence of internal loads, *J. geophys. Res.*, **102**, 2438.

M^cKenzie, D. & Jackson, J., 2002. Conditions for flow in the lower crust, *Tectonics*, **21**, doi:10.1029/2002TC001394.

M^cKenzie, D., Nimmo, F., Jackson, J., Gans, P. & Miller, E., 2000. Characteristics and consequences of flow in the lower crust, *J. geophys. Res.*, **105**, 11 029–11 046.

M^cKenzie, D., Jackson, J. & Priestley, K., 2005. Thermal structure of oceanic and continental lithosphere, *Earth planet. Sci. Lett.*, **233**, 337–349.

McNamara, D., Owens, T., Silver, P. & Wu, F., 1994. Shear wave anisotropy beneath the Tibetan Plateau, *J. geophys. Res.*, **99**, 13 655–13 665.

McNamara, D., Owens, T. & Walter, W., 1995. Observations of regional phase propagation across the Tibetan Plateau, *J. geophys. Res.*, **100**, 22 215–22 229.

Meade, B., 2007. Present-day kinematics at the India–Asia collision zone, *Geology*, **35**, 81–84.

Meissner, R. & Kusznir, N., 1987. Crustal viscosity and the reflectivity of the lower crust, *Ann. Geophysicae, Ser. B*, **5**, 365–373.

Meissner, R., Tilmann, F. & Haines, S., 2004. About the lithospheric structure of central Tibet, based on seismic data from the INDEPTH III profile, *Tectonophysics*, **380**, 1–25.

Mitra, S., Priestley, K., Bhattacharyya, A. & Gaur, V., 2005. Crustal structure and earthquake focal depths beneath Northeastern India and southern Tibet, *Geophys. J. Int.*, **160**, 227–248.

Owens, T. & Zandt, G., 1997. Implications of crustal property variations for models of the Tibetan Plateau evolution, *Nature*, **387**, 37–43.

Ozacar, A. & Zandt, G., 2004. Crustal seismic anisotropy in central Tibet: implications for deformational style and flow in the crust, *Geophys. Res. Lett.*, **31**, L23601.

Royden, L., 1996. Coupling and decoupling of crust and mantle in convergent orogens: implications for strain partitioning in the crust, *J. geophys. Res.*, **101**, 17 679–17 705.

Sandvol, E., Ni, J., Kind, R. & Zhao, W., 1997. Seismic anisotropy beneath the southern Himalayas–Tibet collision zone, *J. geophys. Res.*, **102**, 17 813–17 823.

Saramito, P., Roquet, N. & Etienne, J., 2006. RHEOLEF open-source free software, available at <http://www-lmc.imag.fr/lmc-edp/Pierre.Saramito/rheolef>.

Shapiro, N. & Ritzwoller, M., 2002. Monte-Carlo inversion for a global shear-velocity model of the crust and upper mantle, *Geophys. J. Int.*, **151**, 88–105.

Tapponnier, P., Xu, Z., Roger, F., Meyer, B., Arnaud, N., Wittlinger, G. & Yang, J., 2001. Oblique stepwise rise and growth of the Tibet Plateau, *Science*, **294**, 1671–1677.

Thatcher, W., 2006. Microplate model for present-day deformation of Tibet, *J. geophys. Res.*, **112**, B01401.

Tilmann, F., Ni, J. & INDEPTH, III Seismic Team., 2003. Seismic imaging of the downwelling Indian lithosphere beneath Central Tibet, *Science*, **300**, 1424–1427.

Vanderhaeghe, O., Medvedev, S., Fullsack, P., Beaumont, C. & Jamieson, R., 2003. Evolution of orogenic wedges and continental plateaux; insights from crustal thermal-mechanical models overlying subducting mantle lithosphere, *Int. Geol. Rev.*, **44**, 39–61.

Wei, W. *et al.*, 2001. Detection of widespread fluids in the Tibetan crust by magnetotelluric studies, *Science*, **292**, 716–718.

Yuan, X., Ni, J., Kind, R., Mechie, J. & Sandvol, E., 1997. Lithospheric and upper mantle structure of southern Tibet from a seismological passive source experiment, *J. geophys. Res.*, **102**, 27 491–27 500.

Zhang, P. *et al.*, 2004. Continuous deformation of the Tibetan plateau from global positioning system data, *Geology*, **32**, 809–812.

Zhao, W. *et al.*, 2001. Crustal structure of central Tibet as derived from project INDEPTH wide-angle seismic data, *Geophys. J. Int.*, **145**, 486–498.

APPENDIX: AN ANALYTIC SOLUTION

The analytic solution to the viscous flow problem shown in Fig. 1 is straightforward to obtain if $a = h$ and the shear stress, rather than w , is zero on Γ_5 , because the flow driven by the rigid motion of the top and bottom of the viscous layer does not alter the pressure when gravity is absent. This result allows the solutions that M^cKenzie *et al.* (2000) obtained to a similar problem, to be used to calculate the time-dependent behaviour. All the variables in this Appendix are dimensionless and the primes are omitted.

The thickness of the layer is $\xi - \zeta$, where $\xi(x, t)$ is the upper and $\zeta(x, t)$ is the lower boundary. The kinematic condition requires the rate of change of the thickness of the layer to equal the difference between the top and bottom vertical velocity,

$$\frac{d}{dt}(\xi - \zeta) = w_{z=1} - w_{z=0}. \quad (\text{A1})$$

If the layer is to be isostatically compensated,

$$\zeta = -\left(\frac{1}{R-1}\right)\xi \quad (\text{A2})$$

and eq. (A1) becomes

$$\left(\frac{R}{R-1}\right)\frac{d\xi}{dt} = w_{z=1} - w_{z=0}. \quad (\text{A3})$$

It is convenient to separate p into a lithostatic part, $1 - z$ and a perturbation p_1 ,

$$p = 1 - z + p_1. \quad (\text{A4})$$

Then eqs (5) and (6) become

$$\nabla \cdot \mathbf{v} = 0, \quad (\text{A5})$$

$$\nabla^2 \mathbf{v} = \nabla p_1. \quad (\text{A6})$$

We seek a 2-D solution to these equations using a stream function ψ :

$$\mathbf{v} = (u, w) = \left(-\frac{\partial\psi}{\partial z}, \frac{\partial\psi}{\partial x} \right), \quad (\text{A7})$$

which satisfies eq. (A5). Taking the curl of eq. (A6),

$$\nabla^4\psi = 0. \quad (\text{A8})$$

The boundary conditions become

$$-\left(\frac{\partial\psi}{\partial z} \right)_{z=0,1} = -\frac{1}{Ar}, \quad (\text{A9})$$

$$\sigma_{zz} = 0 = -p_{z=1+\xi} + 2 \left(\frac{\partial^2\psi}{\partial x \partial z} \right)_{z=1}. \quad (\text{A10})$$

Since eq. (A9) requires $\partial\psi/\partial z$ to be constant on both boundaries, eq. (A10) becomes

$$p_{1(z=1)} = \xi. \quad (\text{A11})$$

The shear stress on $x = 0$ requires

$$\left[-\frac{\partial^2\psi}{\partial z^2} + \frac{\partial^2\psi}{\partial x^2} \right]_{x=0} = 0. \quad (\text{A12})$$

Since $u = 0$ on $x = 0$, $(\partial\psi/\partial z)_{x=0} = 0$. Eq. (A12) therefore requires

$$\left[\frac{\partial^2\psi}{\partial x^2} \right]_{x=0} = 0 \quad (\text{A13})$$

or, equivalently,

$$[\nabla^2\psi]_{x=0} = 0. \quad (\text{A14})$$

The pressure p_1 is obtained by integration of eq. (A6)

$$\frac{\partial p_1}{\partial x} = -\nabla^2 \frac{\partial\psi}{\partial z} \quad (\text{A15})$$

or

$$\frac{\partial p_1}{\partial z} = \nabla^2 \frac{\partial\psi}{\partial x}. \quad (\text{A16})$$

A suitable solution to eq. (A8) is

$$\psi = F(x, z) + G(x, z) + \frac{z}{Ar}, \quad (\text{A17})$$

where

$$F(x, z) = (A_1 + B_1x)e^{-k_1x} \cos k_1z,$$

$$G(x, z) = [(A_2 + B_2z)e^{-k_2z} + (C_2 + D_2z)e^{k_2z}] \sin k_2x, \quad (\text{A18})$$

and k_1 and k_2 are the vertical and horizontal wavenumbers, respectively. G is the same function as M^cKenzie *et al.* (2000, eqs A5 and A6) obtained. The condition $\sigma_{xz} = 0$ on $x = 0$ requires $B_1 = 0$, when $\nabla^2 F = 0$ everywhere. eqs (A15) and (A16) then show that p_1 is independent of F and depends only on G . The horizontal velocity

$-\partial\psi/\partial z$ on $z = 0, 1$ is $-1/Ar$ if $\partial F/\partial z$ and $\partial G/\partial z$ are zero on these boundaries. The first condition requires

$$\sin k_1 = 0 \quad \text{or} \quad k_1 = n\pi. \quad (\text{A19})$$

The second leads to the same expressions for rigid boundary conditions discussed by M^cKenzie *et al.* (2000). The boundary condition $u = 0$ on $x = 0$ requires

$$-\frac{1}{Ar} + \sum_{n=1}^{\infty} n\pi A_1(n) \sin n\pi z = 0. \quad (\text{A20})$$

Eq. (A20) requires that $A_1(n) = 0$ if n is even, and

$$A_1(m) = \frac{4}{k_m^2 Ar}, \quad k_m = (2m + 1)\pi, \quad (\text{A21})$$

when $n(=2m + 1)$ is odd. Therefore, the boundary conditions can only be satisfied by discrete values of k_1 . The final boundary condition, eq. (A3), requires

$$\left(\frac{R}{R-1} \right) \frac{d\xi}{dt} = \left(\frac{\partial G}{\partial x} \right)_{z=1} - \left(\frac{\partial G}{\partial x} \right)_{z=0} + H, \quad (\text{A22})$$

where

$$H = \left(\frac{\partial F}{\partial x} \right)_{z=1} - \left(\frac{\partial F}{\partial x} \right)_{z=0} = \frac{8}{Ar} \sum_{m=0}^{\infty} \frac{e^{-k_m x}}{k_m}, \quad (\text{A23})$$

H is a function of x but not of t . Fourier transforming eqs (A22) and (A23) with respect to x gives

$$\left(\frac{R}{R-1} \right) \frac{d\bar{\xi}}{dt} = \left(\frac{\partial \bar{G}}{\partial x} \right)_{z=1} - \left(\frac{\partial \bar{G}}{\partial x} \right)_{z=0} + \bar{H}, \quad (\text{A24})$$

where the bars denote transformed variables. $\bar{\xi}$ and \bar{G} are functions of t , but \bar{H} is a constant. M^cKenzie *et al.* showed that the solution to this equation when $\bar{H} = 0$ is

$$\bar{\xi} = \bar{\xi}_0 e^{-t/\tau} \quad (\text{A25})$$

and obtained expressions for $\tau(k)$. When $\bar{H} \neq 0$, the solution to eq. (A24) is

$$\bar{\xi} = \bar{\xi}_0 (1 - e^{-t/\tau}), \quad (\text{A26})$$

where

$$\bar{\xi}_0 = \left(\frac{R-1}{R} \right) \tau \bar{H}. \quad (\text{A27})$$

The Fourier transforms, to obtain \bar{H} from H using eq. (A23) and $\bar{\xi}(t)$ from $\bar{\xi}(t)$ using eq. (A26), were carried out numerically. The solution is only valid when $\xi, \zeta \ll 1$. Since we are interested in the long wavelength behaviour, we used the expression for τ when $k \ll 1$ for rigid boundary conditions on $z = 0, 1$ (M^cKenzie *et al.* 2000, A22):

$$\tau = \frac{3R}{k^2(R-1)}. \quad (\text{A28})$$